Mechanism and Size Cutoff for Steric Exclusion from Actin-Rich Cytoplasmic Domains

Lee W. Janson, Keith Ragsdale, and Katherine Luby-Phelps
The University of Texas Southwestern Medical Center at Dallas, Dallas, Texas 75235-9040 USA

ABSTRACT Subdomains of the cytoplasmic volume in tissue culture cells exclude large tracer particles relative to small. Evidence suggests that exclusion of the large particles is due to molecular sieving by the dense meshwork of microfilaments found in these compartments, but exclusion as a result of the close apposition of the dorsal and ventral plasma membrane of the cell in these regions has not been ruled out conclusively. In principle, these two mechanisms can be distinguished by the dependence of exclusion on tracer particle size. By fluorescence ratio imaging we have measured the partition coefficient (P/P_0) into excluding compartments for tracer particles ranging in radius from 1 to 41 nm. The decay of P/P_0 as a function of particle radius is better fitted by three molecular sieving models than by a slit pore model. The sieving models predict a percolation cutoff radius of the order of 50 nm for partitioning into excluding compartments.

INTRODUCTION

Much of our current understanding of intracellular biochemistry is extrapolated from the results of studies carried out in dilute solution. As a consequence, the diffusion and partitioning of subcellular components are often assumed to be unrestricted in the absence of binding interactions. However, it is now clear that the diffusion of protein-sized particles is hindered significantly by hydrodynamic interactions with cytoplasmic and cytoskeletal components (Hou et al., 1990; Luby-Phelps et al., 1987). In addition, ratio imaging studies of the distribution of inert, fluorescent tracer particles in well-spread tissue culture cells have revealed the existence of subdomains of the cytoplasmic volume that exclude large particles relative to small (Luby-Phelps and Taylor, 1988; Provance et al., 1993). By whole mount electron microscopy, these regions are readily distinguishable by the absence of mitochondria, endoplasmic reticulum, and other large membrane-bounded organelles. Microtubules and vimentin intermediate filaments are also absent from excluding compartments (Provance et al., 1993). Stereo morphometry and fluorescence intensity measurements suggest that these regions are very thin, with the dorsal and ventral cortices of the cell closely apposed. Ultrastructurally, these compartments thus resemble the growth cones of axons and the leading lamellipodia of migrating cells, which also exclude large tracer particles (Luby-Phelps and Taylor, 1988). Like growth cones and lamellipodia, they contain bundles and meshworks of microfilaments. Staining with fluorescent phallotoxins reveals the presence of actin filaments in the filament bundles, and presumably the meshworks are also composed of F-actin (Provance et al., 1993). Similar actin meshworks have been demonstrated at the electron microscopic level in growth cones and lamellipodia (Bridgman and Daly, 1989; Small et al., 1982).

In unstimulated, interphase fibroblasts and epithelial cells, excluding compartments are very stable, persisting unchanged for several hours. However, there is evidence to suggest that the architecture of these compartments is regulated physiologically. Treatment of growth cones with 50 μM forskolin induces microtubules to invade the excluding compartment at the leading edge. Subsequently, organelles enter the leading edge along the tracks defined by microtubules (Forscher et al., 1987). A similar process occurs when two growth cones come in contact, raising the possibility that excluding compartments in general might be remodeled in response to extracellular signals (Lin and Forscher, 1993). By contrast, in fibroblasts made quiescent by serum starvation, excluding compartments become very prominent, taking up most of the spread area of cell.

Although excluding compartments are a feature of all well-spread tissue culture cells, their function is not well understood. Their ultrastructure is consistent with a mechanical role, and it has been shown that the leading lamellipodia of migrating cells are indeed very stiff (Felder and Elson, 1990). It is clear that membrane-bound protein synthesis or vesicle trafficking on microtubules does not take place in these compartments, because the requisite machinery is absent. However, inasmuch as the percolation cutoff and the mechanism of exclusion are not known it is hard to predict which cellular components do have access to excluding compartments. An answer to this question is of particular importance in formulating detailed models for protrusion of the leading edges of migrating cells and growth cones.

Two possible mechanisms for exclusion are suggested by the available data: The meshwork of filaments in excluding compartments may act as a molecular sieve (Fig. 1 *A*) or particles may be excluded because of the close apposition of the dorsal and ventral cell cortices (Fig. 1 *B*). There is some

Received for publication 17 April 1996 and in final form 31 May 1996.

Address reprint requests to Dr. Katherine Luby-Phelps, University of Texas Southwestern Medical Center, 5323 Harry Hines Boulevard, Dallas, TX 75235-9040. Tel.: 214-648-2190; Fax: 214-648-8685; E-mail: lubyphel@utsw.swmed.edu.

0006-3495/96/09/1228/07 $2.00

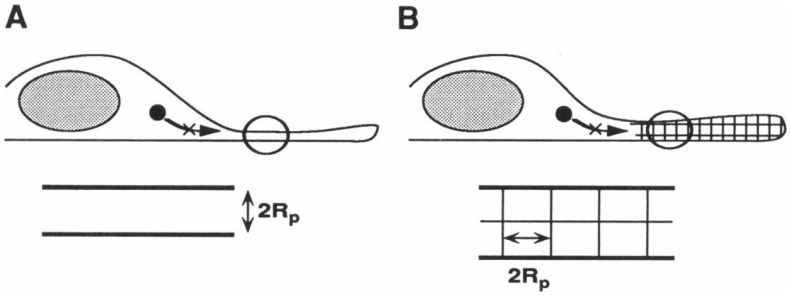

FIGURE 1 Diagrammatic representation of two possible mechanisms for steric exclusion of inert tracer particles from cytoplasmic excluding compartments. Circles denote regions shown at higher magnification below. (*A*) Exclusion by a slit pore with half-width R_p. (*B*) Exclusion by a molecular sieve, depicted here as a square lattice of cytoskeletal fibers with mean pore radius R_p.

evidence against the latter mechanism (Provance et al., 1993), but this has not been tested rigorously. In principle, exclusion by molecular sieving can be distinguished from exclusion by two closely apposed parallel plates (a slit pore) by the dependence of partitioning on particle radius (R). For a slit pore, the partition coefficient (P/P_0) decays as $(1 - R/r_p)$, where r_p is half of the spacing between the parallel plates, whereas for a molecular sieve P/P_0 decays as a higher-order function of R. By ratio imaging, we have measured P/P_0 into excluding compartments for a series of inert, fluorescent tracer particles ranging in radius from 1 to 41 nm. Because hydrophobic or electrostatic interaction of these particles with intracellular components is negligible (Hou et al., 1990), steric hindrance is expected to be the primary determinant of P/P_0. Analysis of the data allows us to rule out a slit pore as the mechanism of exclusion. Applying sieving models of simple geometry, we predict a mean pore radius of ≈50 nm as the percolation cutoff for entry into these compartments.

MATERIALS AND METHODS

Cell culture

Swiss 3T3 cells (CCL 92, American Type Culture, Rockville, MD) were cultured in Dulbecco's Modified Eagle's medium (#31600–034, Gibco BRL, Gaithersburg, MD) as previously described (Provance et al., 1993). Cells were subcultured onto 40-mm round glass coverslips (Custom #40 Cir 1D, Fisher, Pittsburgh, PA) at least 48 h before each experiment to allow them to become well spread. In some cases, cells were made quiescent by being deprived of serum for 24 h or being cultured in 0.2% serum for 48 h before the experiment. For other experiments we obtained populations of oriented, migrating cells by wounding a confluent monolayer 20 min before microinjection.

Fluorescence microscopy

FTC-Ficoll was prepared by amidation, fluoresceination, and size fractionation of Ficoll 400 (Pharmacia, Newark, NJ), as described (Luby-Phelps, 1988). The mean hydrodynamic radius of each size fraction was calculated from the aqueous diffusion coefficient measured by fluorescence recovery after photobleaching (FRAP) (Luby-Phelps et al., 1987). Fractions were lyophilized from distilled water and reconstituted at high concentration in sterile 2.5 mM PIPES, pH 7.0. Cy5-Ficoll was prepared by derivatizing amidated Ficoll 400 with Cy518.OSu (Amersham Life Science, Pittsburgh, PA) followed by size fractionation on Sepharose CL-6B (Pharmacia). The void volume was pooled and concentrated as above. For each experiment an aliquot of 10 kDa rhodamine dextran (#D-1824, Molecular Probes, Eugene, OR) and an aliquot of Cy5-Ficoll were mixed with an aliquot of FTC-Ficoll of a particular radius. The mixture was microinjected into living cells by pressure injection as described previously (Provance et al., 1993). Following a 2–4-h recovery period, coverslips containing injected cells were mounted into a modified Sykes–Moore chamber (Custom Scientific, Dallas, TX) and maintained at 37°C on the stage of a Axiovert 135 fluorescence microscope (Carl Zeiss, Thornwood, NY).

Digital fluorescence imaging and ratio imaging

We acquired rhodamine, fluorescein, and Cy5 fluorescence images at 100× magnification, using a cooled CCD camera (Photometrics, Tucson, AZ) as previously described (Luby-Phelps et al., 1995). Background images at each wavelength were acquired from fields that did not contain injected cells. To minimize the variance of ratio values among the image set for a given size of tracer particle, the background image was normalized to the mean background intensity outside the cell in each image before background subtraction. We calculated floating point ratio images as previously described (Provance et al., 1993), using BDS-Image software (Oncor, Gaithersburg, MD) and a Macintosh IIfx computer.

Data analysis

Regions of interest in each ratio image were defined interactively, and mean ratio values within each region were measured by use of the program BDS-Image. The mean fluorescein/rhodamine ratio values for FTC-Ficoll fractions in excluding and nonexcluding compartments were used to calculate P/P_0 for each size fraction of FTC-Ficoll (described in more detail in Results, below). P/P_0 was plotted as a function of particle radius, and nonlinear least-squares curve fitting was performed with DeltaGraph Pro 3.52 (Deltapoint, Monterey, CA). Simulations of the effects of tracer particle polydispersity on the observed P/P_0 were also carried out with DeltaGraph.

RESULTS

Mapping the distribution of tracer particles in living cells

Mixtures of 10 kDa rhodamine dextran (radius 1 nm), Cy5-Ficoll (radius 35 nm), and a FTC-Ficoll fraction were microinjected into the cytoplasm of living Swiss 3T3 cells. The mean hydrodynamic radius of the FTC-Ficoll was varied from sample to sample, over a range from 1 to 41 nm. Rhodamine dextran, which is not excluded from excluding compartments, was intended as a volume marker to correct for variable path length that was due to the contours of the cell. Cy5-Ficoll was intended to mark excluding compartments by its exclusion. For each cell, digital fluorescence images of each of the three probes were acquired as de-

scribed in Materials and Methods, and two ratio images were generated. The ratio image of the distribution of Cy5-Ficoll relative to the distribution of rhodamine dextran (CY5/RH) was used to map excluding compartments in each cell. The ratio image of FTC-Ficoll to rhodamine-dextran (FTC/RH) was used to map the concentration variations of FTC-Ficoll in the cytoplasmic volume (Fig. 2). Pseudocolor concentration maps of FTC-Ficoll of several sizes in single cells are presented in Fig. 3.

Measurement of partition coefficient

For each cell, excluding compartments and nonexcluding compartments were outlined interactively on the CY5/RH image and saved as a graphic overlay. The overlay was applied to the FTC/RH image of the same cell, and the mean ratio in each region of interest was calculated (see Fig. 2). For each cell, the results for all excluding compartments were averaged and divided by the averaged results for all nonexcluding compartments. Because the ratio values in the FTC/RH image represent relative concentrations of FTC-Ficoll, this gives the partition coefficient (P/P_0) of the particular FTC-Ficoll fraction into excluding compartments. Data from all cells injected with a particular FTC-Ficoll size fraction were averaged to yield a mean P/P_0. The decay of P/P_0 as a function of the mean hydrodynamic radius of each FTC-Ficoll fraction for untreated, interphase cells is shown in Fig. 4. Nearly identical results were obtained for the leading edges of polarized cells migrating into an experimental wound and from cells made quiescent by serum deprivation (data not shown). However, the projected area occupied by excluding compartments in quiescent cells was much greater than in nonquiescent cells, reducing the nonexcluding compartment to narrow, branching channels radiating from the cell center. These channels appeared by phase contrast microscopy as regions of high refractive index.

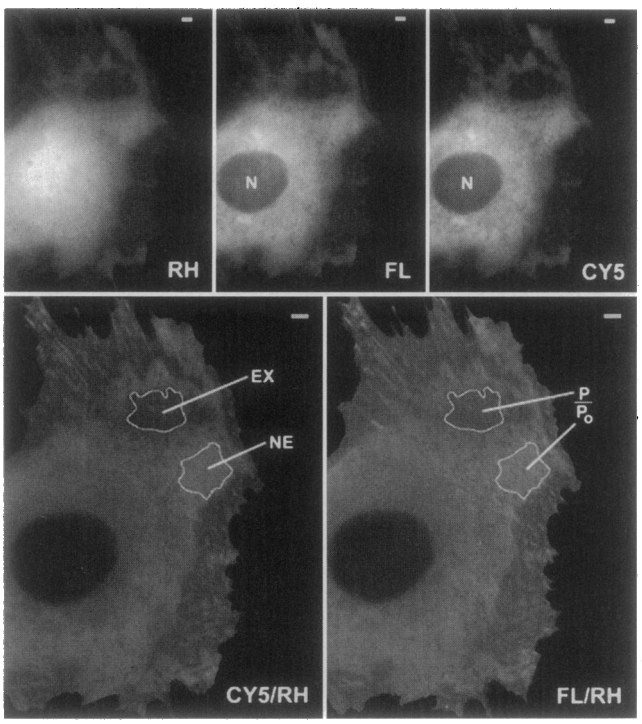

FIGURE 2 Ratio imaging method of obtaining partition coefficients. Background subtracted fluorescence images showing the intensity distributions of 10 kDa rhodamine dextran (*RH*), FTC-Ficoll (*FL*), and Cy5-Ficoll (*CY5*) in a single, living Swiss 3T3 cell. The ratio of the Cy5 image divided by the rhodamine image (*CY5/RH*) was used to map excluding (*EX*) and nonexcluding (*NE*) compartments in the cytoplasmic volume. The ratio of the fluorescein image divided by the rhodamine image (*FL/RH*) was used to map the concentration variations of FTC-Ficoll within the cell. Excluding and nonexcluding compartments were outlined interactively on the CY5/RH image, and the graphic overlay was applied to the FL/RH image. Mean ratio values within each region of interest were used to calculate P/P_0. The mean hydrodynamic radius of FTC-Ficoll microinjected into the cell shown here was 12 nm. Both FTC-Ficoll and Cy5-Ficoll are excluded from the nucleus (*N*). Bar, 5 μm.

DATA ANALYSIS AND MODEL TESTING

For purely steric hindrance, the dependence of the partition coefficient on particle radius (R) is a function of particle shape and pore geometry. Several models for relatively simple geometries have been proposed in the literature. At least four of them appear applicable to the analysis of our data. In partitioning experiments in vitro, Ficolls behave as nearly ideal hard spheres (Deen et al., 1981). For a spherical particle, the partition coefficient into a slit pore, such as a thin region of the cytoplasmic volume, is given by

$$P/P_0 = (1 - R/r_p), \quad (1)$$

where R is the particle radius and r_p is the half-width of the slit (Giddings et al., 1968; Minton, 1992). The partition coefficient into a spherical cavity or a random array of uniform spherical cavities is

$$P/P_0 = (1 - R/r_p)^3, \quad (2)$$

where r_p is the radius of the cavities (Giddings et al., 1968; Minton, 1992). For a cubical particle, the partition coefficient into a cubic lattice of fibers is

$$P/P_0 = \frac{r_{lat}^3 - 3r_{lat}(r_f + r_c)^2 + 2(r_f + r_c)^3}{r_{lat}^3 - 3r_{lat}r_f^2 + 2r_f^3}, \quad (3)$$

where r_{lat} is the half-width of the network unit cube, r_f is the radius of the fibers forming the sides of the unit cube, r_c is the half-width of the cubical particle, and only orientations of the cubic particle parallel or perpendicular to the faces of the unit cube are allowed (Minton, 1992). Given these orientational constraints, the dependence on R for a spherical particle will be the same for $R = r_c$. For partition of a spherical particle into a network of randomly oriented fibers, the partition coefficient is given by

$$P/P_0 = (1/f')\exp(-\pi h(2R + 2r_f)^2/4), \quad (4)$$

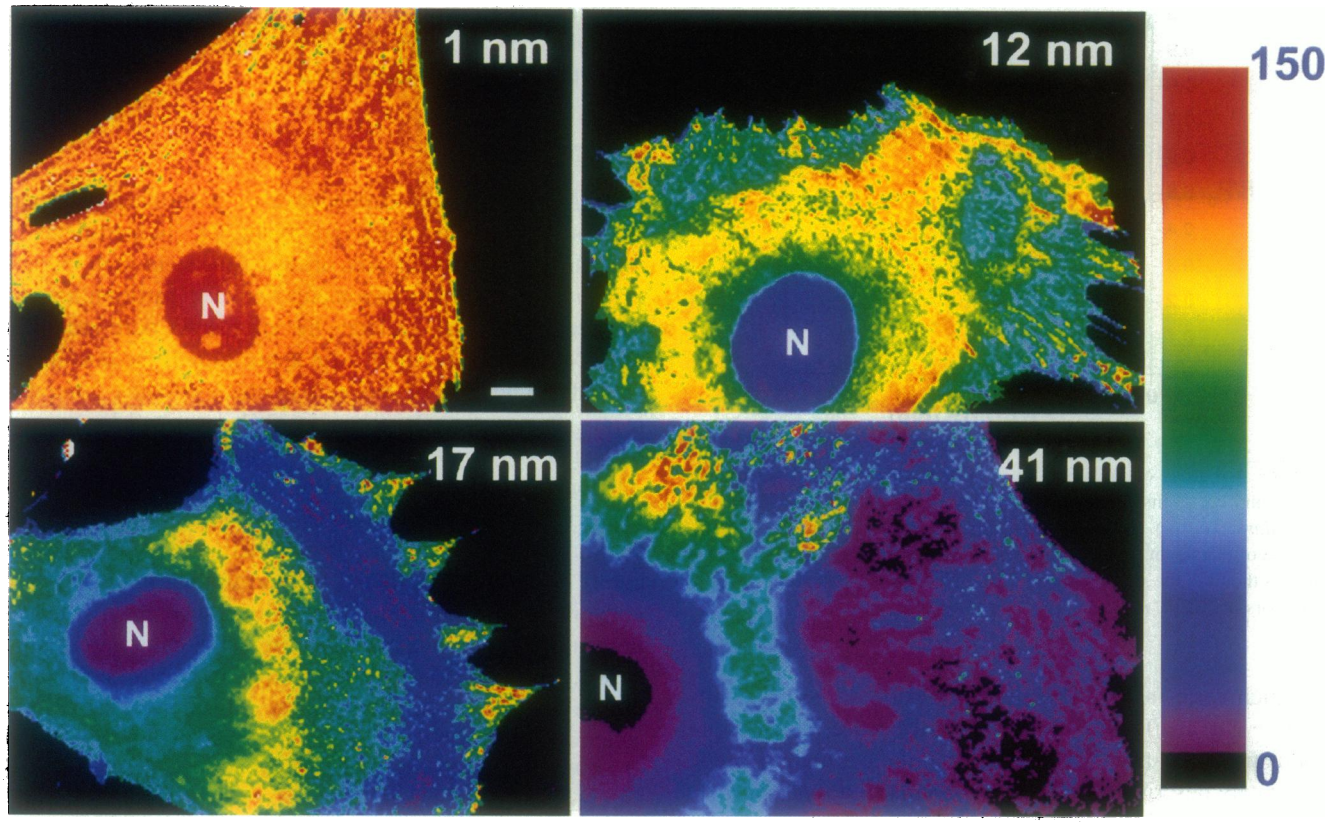

FIGURE 3 Pseudocolor ratio image maps of the intracellular concentration variations for four different fractions of FTC-Ficoll in single, living Swiss 3T3 cells. Relative intensities are encoded as shown by the color wedge at the right. Warm colors are regions of high concentration and cool colors are regions of low concentration. It can be seen that regions of low intensity (excluding compartments) appear and grow in area as the mean radius of particles in the FTC-Ficoll fraction increases. Bar, 10 μm.

where $1/f'$ is the porosity of the network, h is the length of fiber per unit volume, and r_f is the fiber radius (Giddings et al., 1968; Laurent and Killander, 1964; Ogston, 1958). Inasmuch as intersections between fibers in the network are not considered in the random fiber model, this formulation has no percolation cutoff.

The data for P/P_0 as a function of R were fitted to each of the above models by unweighted, nonlinear least squares. The decay of P/P_0 fitted all three sieving models equally well and significantly better than the slit pore model (Fig. 4). The percolation cutoff determined from model 2 is 54 nm, whereas from model 3 it is 34 nm. Values of r_f obtained from models 3 and 4 were similar: 54 nm for the cubic lattice and 37 nm for the random fiber network.

Effect of polydispersity on P/P_0

The value of P/P_0 for $R = 41$ nm is significantly underestimated by any of the fitted curves. Because this particle size is close to the estimated r_p, uncorrected background fluorescence or number fluctuations of the particles in the excluding regions may lead to inaccuracies in determining P/P_0. In addition, because our FTC-Ficoll fractions are moderately polydisperse, the presence of particles of radius smaller than R might lead to an observed P/P_0 greater than predicted for a monodisperse tracer. A Ficoll fraction obtained from size-exclusion chromatography contains a quasi-Gaussian distribution of particle sizes around the mean value of R calculated from the diffusion coefficient measured by FRAP. The standard deviation of this distribution is of the order of 0.14 R (Hou, 1991). The effect of polydispersity on the observed P/P_0 can be calculated as P/P_0 for each size particle in the fraction times its proportional representation in the population, integrated over all particle sizes. For sieving of a Gaussianly distributed population of particles by a random array of uniform spherical cavities

$$P/P_0 = \int_{i=-\infty}^{\infty} \frac{1}{\sigma(2\pi)^{1/2}} \exp(-(r_i - R)^2/2\sigma^2) \cdot (1 - r_i/r_p)^3 \, dr_i, \quad (5)$$

where r_i is the radius of each particle in the population and σ is the standard deviation of the Gaussian distribution of particle sizes. Equation 5 can be solved analytically to give

$$(1 - R/r_p)^3 + A \quad (6)$$

where $A = 3(1 - R/r_p)(\sigma/r_p)^2$. The deviation from the P/P_0 expected for monodisperse tracer particles is thus given by

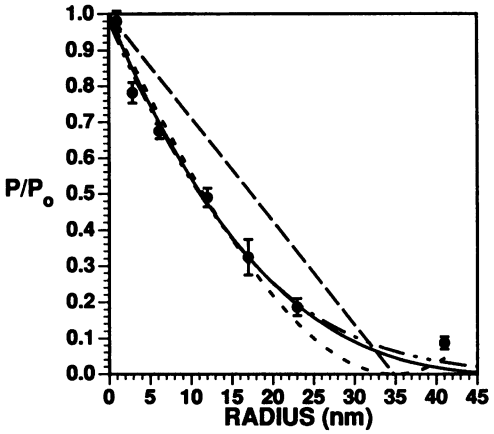

FIGURE 4 Decay of P/P_0 as a function of particle radius. The data are plotted and curve fits to Eqs. 1 (*long-dashed curve*), 2 (*solid curve*), 3 (*short-dashed curve*), and 4 (*dashed–dotted curve*) are shown. The data fit all three of the sieving models (Eqs. 2–4) with $R^2 = 0.99$ and $\chi^2 = 0.01$, whereas the fit to the slit pore model (Eq. 1) had $R^2 = 0.81$ and $\chi^2 = 0.18$. Error bars are SEM, $n \geq 5$.

A, which varies as σ^2. The analytical solution is valid only for $R - 3\sigma \gg 0$ and $R + 3\sigma \gg r_p$. Because the distribution is truncated at $r_i = 0$, for small R the population is not adequately described by the Gaussian distribution. For $R + 3\sigma \geq r_p$, a significant number of the largest particles in the fraction will be excluded from the pores. However, for $R < r_p - 3\sigma$, the equation can be evaluated numerically with $P/P_0 = 0$ for $r_i > r_p$ (Fig. 5, dashed curves). The value of A as a function of R/r_p is shown in Fig. 5 for several values of σ, including $\sigma = 0.14\ R$, which describes the polydispersity of the FTC-Ficoll fractions used in this study. We find that the error in P/P_0 that is due to particle polydispersity accounts for at most 20% of the difference between the observed P/P_0 for FTC-Ficoll with $R = 41$ nm and P/P_0 predicted from the fitted curves.

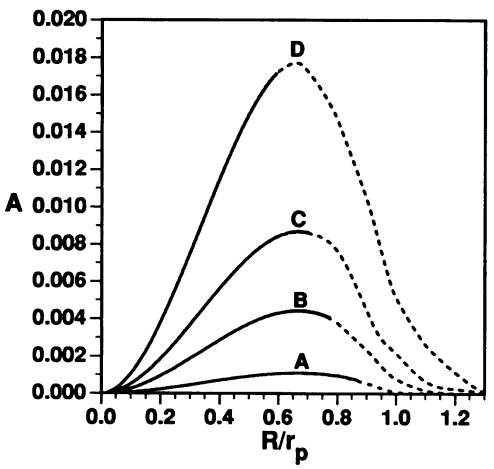

FIGURE 5 Effect of polydispersity of P/P_0. A (see Results) is plotted as a function of R/r_p. Solid curves are derived from the analytical solution to Eq. 5. Dashed curves are splines fitted to values of A determined by numerical evaluation of Eq. 5 for $R > r_p - 3\sigma$. In general the effects of moderate polydispersity are small relative to the measured P/P_0. (A) $\sigma = 0.05\ R$, (B) $\sigma = 0.1\ R$, (C) $\sigma = 0.14\ R$, (D) $\sigma = 0.2\ R$. Curve C corresponds to the polydispersity of the FTC-Ficoll used in this study.

CONCLUSIONS

Our data for the size dependence of partitioning of inert fluorescent tracer particles into excluding compartments in the cytoplasm of living cells are not consistent with models that predict a linear relationship between partitioning and particle radius. This includes the simple slit pore model in which exclusion is due to close apposition of the dorsal and ventral boundaries of the cell in the excluding compartments. In contrast, the data are well described by several molecular sieving models, all of which predict a nonlinear relationship between partitioning and particle radius.

Two of the sieving models allow us to estimate the percolation cutoff of the sieving network: A percolation cutoff of 54 nm is predicted for partitioning into a random network of uniform spherical cavities, whereas a percolation cutoff of 34 nm is predicted for partitioning into a cubic lattice. The partition coefficient that is due to steric hindrance should be the same for a cubical pore and for a spherical pore with an equivalent surface area (Giddings et al., 1968). A sphere with a surface area equivalent to the unit cube of the cubic lattice model has a radius of 47 nm, in good agreement with the results for the network of spherical cavities. The random fiber network model, which does not have a percolation cutoff, is not likely to be completely physiological, as there is a wealth of evidence in the literature (for example, Hartwig and Shevlin, 1986; Schliwa and van Blerkom, 1981) that cytoskeletal filaments make intersections with one another.

We note that the observed P/P_0 for the largest tracer is significantly underestimated by all the models tested. The discrepancy is not completely accounted for by noise in the data or by polydispersity of the particles. Inspection of Figs. 2 and 3 suggests an additional possiblity. The degree of exclusion within an excluding compartment is observed to be heterogeneous on a distance scale smaller than the regions of interest that we used to obtain P/P_0. As the tracer radius approaches the mean pore radius of the excluding compartment, the fluorescence intensity contributed by accessible subdomains with a percolation cutoff greater than the mean will cause P/P_0 to be higher than predicted for a homogeneous excluding compartment. In general we find that the data are well fitted by models in which P/P_0 is the weighted average of exclusion by two discrete subdomains, one of which acts as a molecular sieve. Equally good fits to the data are obtained whether the second subdomain is modeled as a sieve or as slit pore. Fig. 6 shows the best fit to a model in which both subdomains are assumed to be random arrays of spherical cavities and the fractional volume occupied by the first subdomain is arbitrarily chosen to be 0.9.

Analysis of our data indicates that proteins and macromolecular complexes of radius smaller than ≈50 nm can

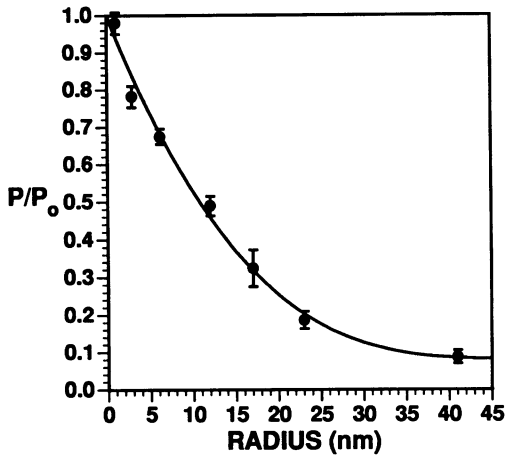

FIGURE 6 Least-squares fit of the data to a model in which P/P_0 is the weighted average of exclusion by two discrete arrays of spherical cavities, each characterized by a uniform pore size. The fractional volume occupied by the first subdomain was arbitrarily chosen to be 0.9. P/P_0 is plotted versus R as in Fig. 4. The equation that best fits the data is $P/P_0 = 0.9(1 - R/46)^3 + 0.1(1 - R/711)^3$, with $R^2 = 0.99$ and $\chi^2 = 6.23 \times 10^{-3}$.

enter excluding compartments. However, as particle size approaches the percolation cutoff, particle concentration may be significantly reduced in the excluding compartments. For example, we would predict that particles the size of a ribosome (radius $\approx$ 15 nm) would be approximately threefold less concentrated in excluding compartments than in nonexcluding compartments. If large particles are present in low abundance, number fluctuations may make the instantaneous concentration in a given compartment even lower than predicted by the nominal P/P_0. The concentration of small molecules such as regulatory metabolites and small globular proteins would be essentially unaffected by steric hindrance. However, the biochemical and physical properties of molecules that do partition into excluding regions might differ significantly from the bulk because of confinement within the pores of the sieving network (Minton, 1992).

Two of the sieving models that we have applied to our data provide information about the radius of the fibers in the sieving network. Both the cubic lattice and the random fiber model suggest that these fibers are of relatively large caliber. Fiber radii estimated from these models were 54 and 37 nm, respectively, comparable with the radii of our largest test particles and considerably larger than any of the three major types of cytoskeletal filament. When fiber radius is constrained to 5 nm, which is the radius of an actin filament (Egelman and Padron, 1984), χ^2 for the best-fitting curve increased twofold to threefold (data not shown). In addition, for the random network of fibers, constraining fiber radius to 5 nm results in a value for length of fiber per unit volume that is $\approx$100 times the physiological concentration of actin (577 mg/ml). Thus, these models suggest that sieving cannot be due simply to a network of single, naked actin filaments. This may indicate that the network fibers are bundles of actin filaments. The relatively large diameter of the fibers could also reflect the association of other cytoplasmic components with actin filaments (Clegg, 1984). Besides various well-known actin-binding proteins, several noncytoskeletal proteins have been shown to bind actin in vitro with reasonable affinity, including protein synthesis elongation factors, neuromodulin, and aldolase (Condeelis, 1995; Hens et al., 1993; O'Reilly and Clarke, 1993). Other proteins and mRNAs have been localized to actin-containing microfilaments in cells (Bassell et al., 1994; Goodnight et al., 1995; Khalil et al., 1995). Theoretical considerations indicate that even very weak associations may lead to adsorption of molecules onto extended surfaces in crowded solutions or confined spaces (Minton, 1994). On the other hand, all the models that we used are greatly simplified compared with the known complexity of cytoarchitecture. More-general models quickly become mathematically intractable. Among the complexities that could make these simple models invalid are nonuniform fiber diameter (for example, actin bundles of various sizes or variations in radius along the length of the fiber), reversible cross-links in the network, nonuniform pore size, and macromolecular crowding, although the effects of the last-named condition appear to be small (Anderson and Quinn, 1974).

We are grateful to Fred Lanni, Allen Minton, and John Phelps for much helpful advice and discussion. We gratefully acknowledge suggestions from the reviewers that significantly improved the manuscript. This research was supported by National Science Foundation grant MCB-9304603.

REFERENCES

Anderson, J. L., and J. A. Quinn. 1974. Restricted transport in small pores: a model for steric exclusion, and hindered particle motion. *Biophys. J.* 14:130–150.

Bassell, G. J., K. L. Taneja, E. H. Kislauskis, C. L. Sundell, C. M. Powers, A. Ross, and R. H. Singer. 1994. Actin filaments and the spatial positioning of mRNAS. [Review.] *Adv. Exp. Med. Biol.* 358:183–189.

Bridgman, P. C., and M. E. Daly. 1989. The organization of myosin and actin in rapid frozen nerve growth cones. *J. Cell Biol.* 108:95–109.

Clegg, J. S. 1984. Properties and metabolism of the aqueous cytoplasm and its boundaries. *Am. J. Physiol.* 246:R133–R151.

Condeelis, J. 1995. Elongation factor 1 alpha, translation and the cytoskeleton. [Review.] *Trends Biochem. Sci.* 20:169–70.

Deen, W. M., M. P. Bohrer, and N. B. Epstein. 1981. Effects of molecular size and configuration on diffusion in microporous membranes. *AIChE J.* 27:952–959.

Egelman, E. H., and R. Padron. 1984. X-ray diffraction evidence that actin is a 100 Å filament. *Nature (Lond.).* 3076:56–58.

Felder, S., and E. Elson. 1990. Mechanics of fibroblast locomotion: quantitative analysis of forces and motions at the leading lamellas of fibroblasts. *J. Cell Biol.* 111:2513–2526.

Forscher, P., L. K. Kaczmarek, J. Buchanan, and S. J. Smith. 1987. Cyclic AMP induces changes in distribution and transport of organelles within growth cones of *Aplysia* bag cell neurons. *J. Neurosci.* 7:3600–3611.

Giddings, J. C., E. Kucera, C. P. Russell, and M. N. Myers. 1968. Statistical theory for the equilibrium distribution of rigid molecules in inert porous networks. *J. Phys. Chem.* 72:4397–4407.

Goodnight, J. A., H. Mischak, W. Kolch, and J. F. Mushinski. 1995. Immunocytochemical localization of eight protein kinase C isozymes overexpressed in NIH 3T3 fibroblasts. Isoform-specific association with microfilaments, Golgi, endoplasmic reticulum, and nuclear and cell membranes. *J. Biol. Chem.* 270:9991–10,001.

Hartwig, J. H., and P. Shevlin. 1986. The architecture of actin filaments and the ultrastructural location of actin-binding protein in the periphery of lung macrophages. *J. Cell Biol.* 103:1007–1020.

Hens, J. J., F. Benfenati, H. B. Nielander, F. Valtorta, W. H. Gispen, and P. N. De Graan. 1993. B-50/GAP-43 binds to actin filaments without affecting actin polymerization and filament organization. *J. Neurochem.* 61:1530–1533.

Hou, L. 1991. Macromolecular diffusion and structural modulation in actin-based reconstituted matrices. Ph.D. thesis. Carnegie-Mellon University, Pittsburgh, PA.

Hou, L., F. Lanni, and K. Luby-Phelps. 1990. Tracer diffusion in F-actin and Ficoll mixtures. Toward a model for cytoplasm. *Biophys. J.* 58: 31–43.

Khalil, R. A., C. B. Menice, C. L. Wang, and K. G. Morgan. 1995. Phosphotyrosine-dependent targeting of mitogen-activated protein kinase in differentiated contractile vascular cells. *Circ. Res.* 76: 1101–1108.

Laurent, T. C., and J. Killander. 1964. A theory of gel filtration and its experimental verification. *J. Chromatogr.* 14:317–330.

Lin, C.-H., and P. Forscher. 1993. Cytoskeletal remodeling during growth cone–target interactions. *J. Cell Biol.* 121:1369–1383.

Luby-Phelps, K. 1988. Fluorescent labeling of polysaccharides. *Methods Cell Biol.* 29:59–73.

Luby-Phelps, K., P. E. Castle, D. L. Taylor, and F. Lanni. 1987. Hindered diffusion of inert tracer particles in the cytoplasm of mouse 3T3 cells. *Proc. Natl. Acad. Sci. USA.* 84:4910–4913.

Luby-Phelps, K., M. Hori, J. Phelps, and D. Won. 1995. Ca^{2+}-regulated dynamic compartmentalization of calmodulin in living smooth muscle cells. *J. Biol. Chem.* 270:21532–21538.

Luby-Phelps, K., and D. L. Taylor. 1988. Subcellular compartmentalization by local differentiation of cytoplasmic structure. *Cell Motil. Cytoskel.* 10:28–37.

Minton, A. P. 1992. Confinement as a determinant of macromolecular structure and reactivity. *Biophys. J.* 63:1090–1100.

Minton, A. P. 1994. Confinement as a determinant of macromolecular structure and reactivity. II. Effects of weakly attractive interactions between confined macrosolutes and confining structures. *Biophys. J.* 68:1311–1322.

O'Reilly, G., and F. Clarke. 1993. Identification of an actin binding region in aldolase. *FEBS Lett.* 321:69–72.

Ogston, A. G. 1958. The spaces in a uniform random suspension of fibers. *Trans. Faraday Soc.* 54:1754–1757.

Provance, D. W., A. MacDowall, M. Marko, and K. Luby-Phelps. 1993. Cytoarchitecture of size-excluding compartments in living cells. *J. Cell Sci.* 106:565–578.

Schliwa, M., and J. van Blerkom. 1981. Structural Interaction of cytoskeletal components. *J. Cell Biol.* 90:222–235.

Small, J. V., G. Rinnerthaler, and H. Hinssen. 1982. Organization of actin meshworks in cultured cells: the leading edge. *In* Organization of the Cytoplasm. Cold Spring Harbor Press, Cold Spring Harbor, NY. 599–623.